

# Local octahedral rotations and octahedral connectivity in epitaxially strained $\text{LaNiO}_3/\text{LaGaO}_3$ superlattices

H. Y. Qi<sup>1</sup> · M. K. Kinyanjui<sup>1</sup> · J. Biskupek<sup>1</sup> · D. Geiger<sup>1</sup> · E. Benckiser<sup>2</sup> · H.-U. Habermeier<sup>2</sup> · B. Keimer<sup>2</sup> · U. Kaiser<sup>1</sup>

Received: 2 March 2015 / Accepted: 4 May 2015 / Published online: 8 May 2015  
© Springer Science+Business Media New York 2015

**Abstract** For  $\text{ABO}_3$  perovskites, octahedral rotations and distortions couple strongly to the functional properties. However, in short period perovskite superlattices, the characterization of the octahedral behavior remains challenging due to the local structural variations of the  $\text{BO}_6$  octahedra. By aberration-corrected high-resolution transmission electron microscopy, we investigated the local octahedral rotations in a  $[(4 \text{ unit cell (u.c.)}/4 \text{ u.c.)} \times 8]$   $\text{LaNiO}_3/\text{LaGaO}_3$  superlattice grown on a (001)  $\text{SrTiO}_3$  substrate. The octahedral behavior varies along the growth direction even though the superlattice is coherently strained. Near the substrate, octahedral rotations about [100] and [010] axes in the superlattice are suppressed due to the octahedral connectivity—rotational magnitudes and patterns—between the  $\text{NiO}_6$  and  $\text{TiO}_6$  octahedra. Away from the substrate, the magnitudes of [100] and [010] rotations are enhanced as a response to substrate-induced tensile strain. Near the surface of the superlattice, the [100] and [010] rotational magnitudes of  $\text{NiO}_6$  and  $\text{GaO}_6$  relax to the bulk values of  $\text{LaNiO}_3$  and  $\text{LaGaO}_3$ , respectively. Our results indicate that the response of octahedral rotations to epitaxial strain in superlattices is significantly different from that in thin films.

## Introduction

$\text{ABO}_3$  perovskites exhibit fascinating functionalities such as colossal magnetoresistance, metal–insulator transitions, multiferroicity, and superconductivity due to the strong correlation between charge, spin, and orbital degrees of freedom [1, 2]. Heterostructures of different  $\text{ABO}_3$  perovskites provide the possibility to not only manipulate the existing functionalities but also create new ones which are enabled by structural and electronic reconstructions at the heterointerfaces [3–5]. It has been demonstrated that the electronic and magnetic properties of  $\text{ABO}_3$  perovskites are strongly coupled to the B–O bond lengths and O–B–O bond angles; therefore, precise control of the  $\text{BO}_6$  octahedral rotations and distortions by epitaxial strain and interfacial octahedral connectivity has become the key to engineering desired functionalities in  $\text{ABO}_3$  perovskite heterostructures [6–22]. One example is the design of new high- $T_c$  superconductors. It has been predicted that epitaxial strain and quantum confinement can be used to manipulate the electronic structure of  $\text{LaNiO}_3/\text{RXO}_3$  superlattices (R = rare earth cation, X = trivalent cation such as Al, Ga...) to match that of cuprate high- $T_c$  superconductors [23]. In bulk  $\text{LaNiO}_3$ , the electron configuration of the  $\text{Ni}^{3+}$  ions is  $t_{2g}^6 e_g^1$  with the  $e_g$  electron occupying either  $d_{x^2-y^2}$  or  $d_{3z^2-r^2}$  orbital. Substrate-induced tensile strain increases the in-plane Ni–O bond lengths thus favors the occupation of the in-plane  $d_{x^2-y^2}$  orbital. The in-plane orbital polarization of the  $e_g$  electron is further supported by the insulating  $\text{RXO}_3$  layers which block the  $c$ -axis charge transfer. Subsequent experiments have revealed orbital polarization, metal–insulator transition, and antiferromagnetism in epitaxial-strained  $\text{LaNiO}_3/\text{RXO}_3$  superlattices [24–27]. However, superconductivity has not

**Electronic supplementary material** The online version of this article (doi:10.1007/s10853-015-9077-y) contains supplementary material, which is available to authorized users.

✉ H. Y. Qi  
haoyuan.qi@uni-ulm.de

<sup>1</sup> Central Facility of Electron Microscopy, Electron Microscopy Group of Materials Science, University of Ulm, Albert Einstein Allee 11, 89081 Ulm, Germany

<sup>2</sup> Max Planck Institute for Solid State Research, Heisenbergstrasse 1, 70569 Stuttgart, Germany

been observed yet and discrepancies between experimental observations and first-principle calculations still persist. Moreover, the local structure of the  $\text{NiO}_6$  octahedral network embedded in epitaxially-strained  $\text{LaNiO}_3/\text{RXO}_3$  superlattices as well as the relation between local structure variations and the resulting properties remains unresolved. Therefore, a detailed determination of the  $\text{NiO}_6$  octahedral rotations is needed in order to provide first, a deeper understanding of the correlation between observed properties and underlying structures and second, a better insight into how to manipulate  $\text{NiO}_6$  octahedral rotations and distortions such that material properties can be engineered in a more controllable way, and third, a more realistic model for first-principle calculations of epitaxially-strained  $\text{LaNiO}_3/\text{RXO}_3$  superlattices.

The characterization of octahedral rotations in perovskite superlattices is challenging since superlattices typically consist of two or more constituent materials. In bulk, each material possesses its own octahedral rotation pattern and magnitudes. In superlattices, the octahedral rotations in each constituent layer are not only affected by their individual response to epitaxial strain but also constrained by octahedral connectivity—rotational magnitudes and patterns—at every heterointerface [16–21]. The effect of interfacial octahedral connectivity in thin films has been reported to be short-ranged which is typically less than 10 unit cells [16–21]. But in short period superlattices where the thickness of each constituent layer is below this range (only a few unit cells), how octahedral connectivity at heterointerfaces affects the octahedral rotations in each constituent layer is still not fully understood. To reveal such a short-range effect, atomic-scale structural determination is indispensable. Synchrotron X-ray diffraction (XRD) has been successful in determining the average octahedral rotation patterns and magnitudes in perovskite thin films as well as in superlattices [9–14]. However, due to the spatial-averaging nature of XRD, it is extremely difficult to investigate local octahedral rotations within the superlattices. Aberration-corrected high-resolution imaging and electron diffraction techniques on the other hand have been successfully used to investigate local octahedral rotations in perovskites at very high spatial resolution. These techniques include annular bright-field (ABF) imaging in aberration-corrected scanning transmission electron microscopy (AC-STEM) [16–20], position-averaged convergent beam electron diffraction (PACBED) in AC-STEM [21, 22], and aberration-corrected high-resolution transmission electron microscopy (AC-HRTEM) [28–31].

In this paper, we present investigations of an epitaxially-strained  $\text{LaNiO}_3/\text{LaGaO}_3$  superlattice grown on a  $\text{SrTiO}_3$  substrate by AC-HRTEM. The structure of the  $\text{TiO}_6$ – $\text{NiO}_6$ – $\text{GaO}_6$  octahedral network was resolved with atomic resolution enabling precise analysis of the local octahedral

rotations. Both epitaxial strain and interfacial octahedral connectivity were found to play an important role in determining the octahedral behavior in the  $\text{LaNiO}_3/\text{LaGaO}_3$  superlattice. We found that the [100] and [010] rotational magnitudes of  $\text{NiO}_6$  and  $\text{GaO}_6$  relax to the bulk values of  $\text{LaNiO}_3$  and  $\text{LaGaO}_3$  even though the superlattice is coherently strained. The observed octahedral behavior in our superlattice is significantly different from that in thin films where epitaxial strain effectively modifies octahedral rotations throughout the entire films [9, 10, 12, 22].

## Experimental

A [(4 u.c./4 u.c.)  $\times$  8]  $\text{LaNiO}_3/\text{LaGaO}_3$  superlattice with a total thickness of  $\sim 250$  Å was grown on a (001)  $\text{SrTiO}_3$  substrate by pulsed laser deposition. The superlattice was deposited by focusing a KrF excimer laser with 2-Hz pulse rate and  $1.6\text{-J}/\text{cm}^2$  energy density onto stoichiometric targets of  $\text{LaNiO}_3$  and  $\text{LaGaO}_3$ . The deposition was carried out in 0.5-mbar oxygen atmosphere at 730 °C. After deposition, the superlattice was annealed in 1-bar oxygen atmosphere at 690 °C for 30 min. More details of sample growth can be found in Ref. [25]. For TEM investigations; cross-sectional specimens were prepared using standard techniques. The specimens were ground to a thickness of 40  $\mu\text{m}$  and subsequently dimpled from both sides to less than 3  $\mu\text{m}$ . The depth of the sphere-shaped deepening was approximately 20  $\mu\text{m}$  so that lower inclination angles could be used during ion milling. In order to avoid any contact of the specimen with water, ethanol was used during the mechanical thinning process. Ion milling was conducted in a Fischione Ion Mill 1010. The milling voltage of the  $\text{Ar}^+$  beam was maintained at 4 kV. The inclination angle was kept at a low value of 7° to increase the area of electron transparency. Throughout the ion milling process, the sample stage was cooled by liquid nitrogen to reduce ion-bombardment-induced amorphisation. High-resolution imaging was performed on an image-side  $C_s$ -corrected FEI Titan 80–300 microscope operated at an acceleration voltage of 300 kV. Negative  $C_s$  imaging (NCSI) conditions were applied to enhance the contrast of the oxygen columns and to reduce delocalization [32–34]. The spherical aberration coefficient  $C_s$  was tuned to  $\sim -15$   $\mu\text{m}$  and the images were acquired with defocus of  $\sim +5$  nm (i.e., overfocus). AC-HRTEM image simulation was carried out using multislice algorithm in QSTEM software.

## Octahedral rotations and [110] projection

To systematically describe the octahedral rotations, Glazer notation was used [35]. Bulk  $\text{LaNiO}_3$  has a rhombohedral

$a^-a^-a^-$  rotation pattern. The sequence of symbols corresponds to rotations about the pseudocubic [100], [010] and [001] axes, respectively (see Fig. 1a). The identical characters indicate same rotation angles about each axis ( $\alpha = \beta = \gamma = 5.2^\circ$ ) [36]. The superscript ( $-$ ) stands for out-of-phase rotations of the adjacent octahedra along the corresponding axis. Bulk  $\text{LaGaO}_3$  has an orthorhombic  $a^-a^-c^+$  rotation pattern with  $\alpha = \beta = 6.17^\circ$  and  $\gamma = 6.22^\circ$  [37], while bulk  $\text{SrTiO}_3$  has a cubic structure which lacks octahedral rotations ( $a^0a^0a^0$ ). Since the superlattice is tensilely strained with respect to a cubic substrate ( $a_{\text{LaNiO}_3, \text{pseudocubic}} = 3.838 \text{ \AA}$ ,  $a_{\text{LaGaO}_3, \text{pseudocubic}} = 3.892 \text{ \AA}$ ,  $a_{\text{SrTiO}_3, \text{cubic}} = 3.905 \text{ \AA}$ ), the [100] and [010] directions are identical. Thus,  $\alpha = \beta$ , which results in an  $a^-a^-c^-$  rotation pattern [9, 13, 14, 22]. Because the octahedra have out-of-phase rotations along the [100] and [010] axes, it is difficult to observe them in either direction [14]. Therefore, cross-sectional TEM specimens were prepared in [110] projection from which the octahedral rotations can be imaged. Figure 1b shows the simulated image of bulk  $\text{LaNiO}_3$  in pseudocubic [110] projection

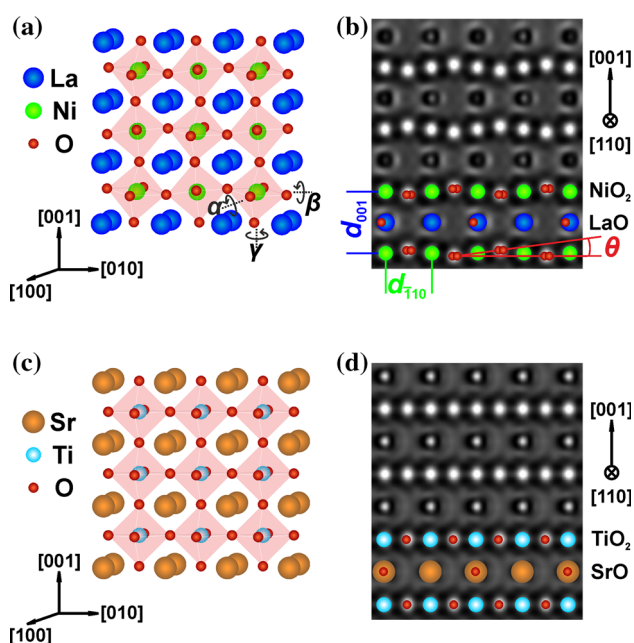


**Fig. 1** **a** Atomic model of bulk  $\text{LaNiO}_3$ . **b** Simulated 300 kV AC-HRTEM image of bulk  $\text{LaNiO}_3$  in [110] projection. The identities of the atomic columns are indicated on the simulation. Multislice method was used with following parameters: spherical aberration coefficient  $C_s = -15 \mu\text{m}$ , defocus  $\Delta f = +5 \text{ nm}$  (i.e., overfocus), sample thickness  $t = 5 \text{ nm}$ , twofold astigmatism  $A_1 = 1 \text{ nm}$ , threefold astigmatism  $A_2 = 50 \text{ nm}$ , coma  $B_2 = 30 \text{ nm}$ , beam convergence angle  $0.3 \text{ mrad}$ , and focal spread  $2 \text{ nm}$ .  $\theta$ ,  $d_{001}$ , and  $d_{110}$  indicate the structural parameters that can be measured from AC-HRTEM images. **c** Atomic model of bulk  $\text{SrTiO}_3$ . **d** Simulated 300 kV AC-HRTEM image of bulk  $\text{SrTiO}_3$  in [110] projection. Simulation parameters are the same as those in (b)

under negative  $C_s$  imaging (NCSI) conditions. All atomic columns appear bright on a dark background with the oxygen and nickel columns showing higher contrast. In pseudocubic [110] projection, the out-of-plane spacing corresponds to the out-of-plane lattice parameter  $d_{001}$  while the in-plane spacing  $d_{110}$  is related to the in-plane lattice parameters  $d_{100}$  and  $d_{010}$  through the following equation  $d_{100} = d_{010} \approx \sqrt{2}d_{110}$ . Due to  $\text{NiO}_6$  octahedral rotations, the projected oxygen positions shift up and down about the horizontal Ni–Ni line forming zigzags in the projections of  $\text{NiO}_2$  layers. To quantify the zigzags, i.e., rotational magnitudes of  $\text{NiO}_6$ , we have defined an angle  $\theta$  whose value is mainly determined by the magnitudes of [100] and [010] rotations, i.e.,  $\alpha$  and  $\beta$ . Rotations about the [100] and [010] axes displace the oxygen anions in a direction along the [001] axis and obviously alter their projected positions. However, rotations about the [001] axis displace the oxygen anions in a direction perpendicular to the [001] axis and thus have a minor effect on the projection. Due to the limitation imposed by projection, the variation of  $\theta$  can only reflect the change of  $\alpha$  and  $\beta$  but not  $\gamma$ . Figure 1c presents the atomic model of bulk  $\text{SrTiO}_3$ . It has a cubic perovskite structure with no octahedral rotations ( $\alpha = \beta = \gamma = 0$ ) and the oxygen anions are located at the face centers of the cubic unit cell. When viewed in [110] direction, the projection of the oxygen anions and titanium cations is in the same horizontal line giving  $\theta = 0$  (see Fig. 1d).

### Analysis of observations

Figure 2a shows an experimental AC-HRTEM image recorded across the substrate–superlattice interface. The in-plane  $\text{BO}_2$  layers ( $B = \text{Ti}/\text{Ni}/\text{Ga}$ ) are marked by the black arrows. The projections of the oxygen octahedra and the B-site cations can be clearly identified. In the lower part of the image, no zigzags were observed in the  $\text{BO}_2$  layers corresponding well to the simulated  $\text{SrTiO}_3$  structure (see Fig. 1d). In the upper part of the image, obvious zigzags can be seen due to the rotations of  $\text{NiO}_6$  and  $\text{GaO}_6$  octahedra. Figure 2b presents the measured structural parameters  $\theta$ ,  $d_{001}$ , and  $d_{110}$ . They are expressed as functions of the number of  $\text{BO}_2$  layers (i.e., unit cells). As highlighted between the solid yellow lines in Fig. 2b, at the  $\text{SrTiO}_3$ – $\text{LaNiO}_3$  interfacial region, we observed a continuous increase of  $\theta$  as well as a continuous decrease of the out-of-plane lattice parameter  $d_{001}$  along the growth direction. The gradual increase of  $\theta$  near the  $\text{SrTiO}_3$ – $\text{LaNiO}_3$  interface can be explained by the interfacial connectivity of the corner-sharing octahedral network. In  $\text{SrTiO}_3$ , due to the lack of octahedral rotations, the oxygen anions are at the face centers of the cubic unit cell. In order to allow octahedral

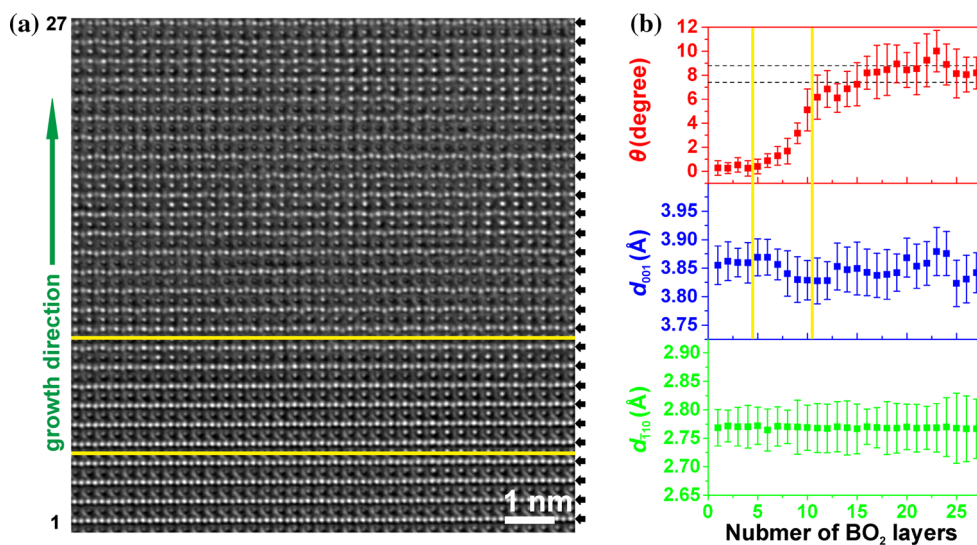


**Fig. 2** **a** 300 kV AC-HRTEM images in [110] projection across the substrate–superlattice interface. The image was acquired using negative  $C_s$  imaging (NCSI) conditions with  $C_s \sim -15 \mu\text{m}$  and defocus  $\sim +5 \text{ nm}$  (i.e., overfocus). Average background subtraction filtering was applied to remove noise. The  $\text{BO}_2$  layers are marked by the black arrows. Numbering of the  $\text{BO}_2$  layers starts from the bottom of each image and increases in the growth direction. **b** Measured

structural parameters  $\theta$ ,  $d_{001}$ , and  $d_{110}$  from (a). Each data point is the average over a distance of  $\sim 10 \text{ nm}$  in one  $\text{BO}_2$  layer with the error bar representing the standard deviation. The dashed lines represent the bulk values of  $\text{LaNiO}_3$  and  $\text{LaGaO}_3$  ( $\theta_{\text{bulkLaNiO}_3} = 7.4^\circ$ ,  $\theta_{\text{bulkLaGaO}_3} = 8.8^\circ$ ). The  $\text{SrTiO}_3$ – $\text{LaNiO}_3$  interfacial region is highlighted between the yellow solid lines in (a, b). Growth directions are indicated by the green arrows (Color figure online)

rotations about the [100] and [010] axes, oxygen anions must be shifted away from the face centers. However, when  $\text{LaNiO}_3$  is epitaxially grown on  $\text{SrTiO}_3$ ,  $\text{NiO}_6$  octahedra are connected to the  $\text{TiO}_6$  ones via the face-centered oxygen anions. As a result of this geometric constraint,  $\text{NiO}_6$  rotations about the [100] and [010] axes are suppressed at the  $\text{SrTiO}_3$ – $\text{LaNiO}_3$  interface. The suppression of the [100] and [010] rotations results in small rotation angles  $\alpha$  and  $\beta$ . Therefore,  $\theta$  is also constrained near the  $\text{SrTiO}_3$  substrate. Moving away from the substrate, the magnitudes of [100] and [010] rotations gradually increase resulting in a continuous increase of  $\theta$ . The continuous decrease of out-of-plane lattice parameter  $d_{001}$  is caused by the difference in lattice parameters of  $\text{SrTiO}_3$  and  $\text{LaNiO}_3$  ( $d_{001,\text{bulkSrTiO}_3} = 3.905 \text{ \AA}$ ,  $d_{001,\text{bulkLaNiO}_3} = 3.838 \text{ \AA}$ ). The measured  $d_{001}$  of  $\text{SrTiO}_3$  is slightly smaller than its bulk value ( $\sim 1 \%$ ) which is within the error range of our instrument. As shown in the lowest panel of Fig. 2b,  $d_{110}$  remains constant as a result of coherent epitaxial growth. Since the electronic structure of  $\text{LaNiO}_3$  is strongly coupled to the Ni–O–Ni bond angles and Ni–O bond lengths, octahedral connectivity at the  $\text{SrTiO}_3$ – $\text{LaNiO}_3$  interface may notably change the electronic and magnetic properties of  $\text{LaNiO}_3$ . In fact, Moon et al. have demonstrated that the functionalities of  $\text{La}_{2/3}\text{Sr}_{1/3}\text{MnO}_3$  ultrathin films can deviate significantly due to the interfacial connectivity with substrates having different octahedral rotation patterns and magnitudes [38]. After the gradual increase,  $\theta$  reaches a plateau. For most layers farther away

from the substrate, i.e., layer 16–27 in Fig. 2b, the values of  $\theta$  exceed that of bulk  $\text{LaNiO}_3$  and some are higher than that of bulk  $\text{LaGaO}_3$ . The increased  $\theta$  agrees with the enhanced magnitudes of [100] and [010] rotations as a response to tensile strain [9, 10, 12, 22]. May et al. have reported  $\alpha = \beta = 7.1 \pm 0.2^\circ$  and  $\gamma = 0.3 \pm 0.7^\circ$  for a  $173 \text{ \AA}$ -thick  $\text{LaNiO}_3$  film grown on  $\text{SrTiO}_3$  substrate which gives  $\theta \sim 10.2^\circ$  [9].

Figure 3a presents an experimental AC-HRTEM image acquired near the superlattice surface. The measured  $\theta$ ,  $d_{001}$ , and  $d_{110}$  are shown in Fig. 3b. The bulk values of  $\text{LaNiO}_3$  and  $\text{LaGaO}_3$  are indicated by the dashed lines. Near the superlattice surface,  $\theta$  oscillates between the bulk values of  $\text{LaNiO}_3$  and  $\text{LaGaO}_3$ . The period of the oscillation is 8 layers corresponding well to the 4 u.c.  $\text{LaNiO}_3/4$  u.c.  $\text{LaGaO}_3$  superlattice structure. Since  $\theta$  is mainly determined by  $\alpha$  and  $\beta$ , our results indicate that near the superlattice surface the magnitudes of [100] and [010] octahedral rotations in  $\text{LaNiO}_3$  and  $\text{LaGaO}_3$  relax toward their own bulk values. At the same time, the connectivity of the octahedral network must be maintained at every  $\text{LaNiO}_3$ – $\text{LaGaO}_3$  interface thus causing the oscillation of  $\theta$ . The out-of-plane lattice parameter in  $\text{ABO}_3$  perovskites can be expressed as  $d_{001} = 2 d_{\text{B-O}} \cos\alpha \cos\beta$ , where  $d_{\text{B-O}}$  is the out-of-plane B–O bond length [35]. When  $\alpha$  and  $\beta$  relax toward bulk values,  $d_{001}$  relaxes as well.

The relaxation of [100] and [010] rotational magnitudes suggests that the response of octahedral rotations to

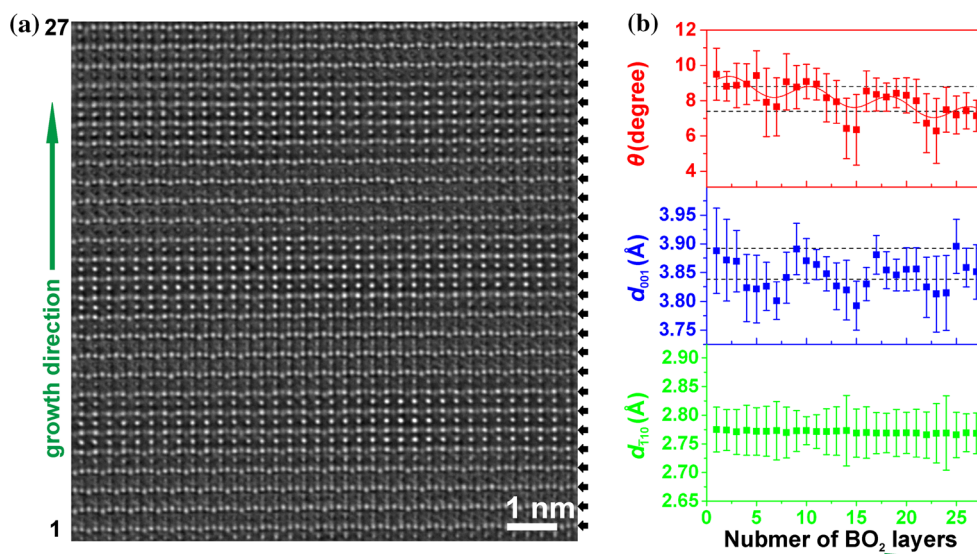


**Fig. 3** **a** 300 kV AC-HRTEM images in [110] projection near the superlattice surface. The image was acquired using negative  $C_s$  imaging (NCSI) conditions with  $C_s \sim -15 \mu\text{m}$  and defocus  $\sim +5 \text{ nm}$  (i.e., overfocus). Average background subtraction filtering was applied to remove noise. The BO<sub>2</sub> layers are marked by the *black arrows*. Numbering of the BO<sub>2</sub> layers starts from the bottom of each image and increases in the growth direction. **b** Measured structural parameters  $\theta$ ,  $d_{001}$ , and  $d_{110}$  from (a). Each data point is the average over

a distance of  $\sim 10 \text{ nm}$  in one BO<sub>2</sub> layer with the *error bar* representing the standard deviation. The *dashed lines* represent the bulk values of LaNiO<sub>3</sub> and LaGaO<sub>3</sub> ( $\theta_{\text{bulkLaNiO}_3} = 7.4^\circ$ ,  $\theta_{\text{bulkLaGaO}_3} = 8.8^\circ$ ,  $d_{001,\text{bulkLaNiO}_3} = 3.838 \text{ \AA}$ ,  $d_{001,\text{bulkLaGaO}_3} = 3.892 \text{ \AA}$ ). The curve in the *top panel* of (b) serves as guide to the eye to emphasize the oscillation of  $\theta$ . Growth directions are indicated by the *green arrows* (Color figure online)

epitaxial strain in superlattices is significantly different from that in thin films. It has been reported that epitaxial strain can effectively modify the octahedral rotations throughout the entire thin films [9, 10, 12, 22]. However, in superlattices, the length scale over which the rotational magnitudes can be controlled by epitaxial strain is much shorter. The octahedral rotations in each constituent layer tend to relax toward the bulk magnitudes. Note that within the error range,  $d_{110}$  near the superlattice surface is the same as that near the substrate meaning that the superlattice is still coherently strained. Therefore, strain relaxation is not likely to be the origin of the bulk-like octahedral rotations. Similar relaxation of octahedral rotations under coherent strain was also reported in a [(4 u.c.//3 u.c.)  $\times$  3] LaNiO<sub>3</sub>/SrTiO<sub>3</sub> superlattice grown on a (001) (LaAlO<sub>3</sub>)<sub>0.3</sub>(SrAl<sub>0.5</sub>Ta<sub>0.5</sub>O<sub>3</sub>)<sub>0.7</sub> substrate investigated by PACBED [21]. However, enhanced [100] and [010] rotational magnitudes of the NiO<sub>6</sub> octahedra were found in a 50 Å-thick LaNiO<sub>3</sub> film grown on the same substrate [22].

By comparing the variations of  $\theta$  in Figs. 2b and 3b, we see clearly that the structure of the octahedral network near the substrate differs from that near the superlattice surface indicating variations in the electronic and magnetic properties along the growth direction. Therefore, in order to produce LaNiO<sub>3</sub>/RXO<sub>3</sub> superlattices with controlled and homogeneous functional properties throughout the entire superlattice, it is necessary to fine-tune the rotational

magnitudes of NiO<sub>6</sub> in every LaNiO<sub>3</sub> layer. Since the NiO<sub>6</sub> rotations are constrained at the SrTiO<sub>3</sub>–LaNiO<sub>3</sub> and LaNiO<sub>3</sub>–LaGaO<sub>3</sub> interfaces, local manipulation of the NiO<sub>6</sub> rotations may be achieved by choosing appropriate RXO<sub>3</sub> materials and substrates. When choosing the RXO<sub>3</sub> materials, rotation patterns and magnitudes of the XO<sub>6</sub> octahedra should be one of the main considerations. Through octahedral connectivity at LaNiO<sub>3</sub>–RXO<sub>3</sub> interfaces, the magnitudes of XO<sub>6</sub> rotations could propagate into the LaNiO<sub>3</sub> layers. Since the effect of interfacial octahedral connectivity is short-ranged, it is reasonable to reduce the thickness of LaNiO<sub>3</sub> layers to avoid the relaxation of the NiO<sub>6</sub> rotations. Meanwhile, the thickness of RXO<sub>3</sub> layers should be increased so that the MO<sub>6</sub> rotations could reach the bulk magnitudes and stabilize the NiO<sub>6</sub> rotations at the next interface. It has been reported in (n u.c.//m u.c.) LaNiO<sub>3</sub>/SrMnO<sub>3</sub> superlattices, the average octahedral rotational magnitudes can be adjusted by altering the superlattice composition [ $n/(n + m)$ ] [13]. When choosing the substrates, the in-plane lattice parameter should be the primary concern to control the in-plane Ni–O bond lengths. A buffer layer can also be inserted to adjust the octahedral rotation pattern and magnitudes before the growth of LaNiO<sub>3</sub>. For instance, Kan et al. have reported that in SrRuO<sub>3</sub>/BaTiO<sub>3</sub>/GdScO<sub>3</sub> heterostructures, the RuO<sub>6</sub> rotations in SrRuO<sub>3</sub> films can be largely reduced by inserting a 1 u.c. thick BaTiO<sub>3</sub> between the SrRuO<sub>3</sub> film and

the GdScO<sub>3</sub> substrate [17]. Note that the present discussion is limited to structural manipulation. Other factors such as the band-gap of RXO<sub>3</sub> and polar discontinuity at heterointerfaces should also be taken into account.

## Summary

We studied the local octahedral rotations in a tensile-strained short period LaNiO<sub>3</sub>/LaGaO<sub>3</sub> superlattice. By AC-HRTEM, local octahedral rotations were probed with atomic resolution. We found that the magnitudes of octahedral rotations about the [100] and [010] axes were largely suppressed near the SrTiO<sub>3</sub> substrate. Enhanced [100] and [010] rotations, which were expected due to tensile strain, were only observed in a short length scale. The magnitudes of the [100] and [010] rotations relax toward their bulk values even though the superlattice is still coherently strained to the substrate. Therefore, in superlattices, epitaxial strain alone is not sufficient to stabilize certain octahedral rotation pattern and magnitudes throughout the entire superlattice. In order to produce LaNiO<sub>3</sub>/RXO<sub>3</sub> superlattices with controlled and homogeneous functionalities, the potential of octahedral connectivity at heterointerfaces should be further exploited.

**Acknowledgements** We are grateful to Sabine Grözinger for cross-section TEM sample preparation. We gratefully acknowledge the financial support by the German Research Foundation (DFG) and the Ministry of Science, Research and the Arts (MWK) of the state Baden-Württemberg within the DFG: KA 1295/17-1 Project.

**Conflict of interest** The authors declare that they have no conflict of interest.

## References

- Imada M, Fujimori A, Tokura Y (1998) Metal-insulator transitions. *Rev Mod Phys* 70:1039–1263
- Tokura Y, Nagaosa N (2000) Orbital physics in transition-metal oxides. *Science* 288:462–468
- Mannhart J, Schlom DG (2010) Oxide interfaces: an opportunity for electronics. *Science* 327:1607–1611
- Hwang HY, Iwasa Y, Kawasaki M, Keimer B, Nagaosa N, Tokura Y (2012) Emergent phenomena at oxide interfaces. *Nat Mater* 11:103–113
- Yu P, Chu YH, Ramesh R (2012) Oxide interfaces: pathways to novel phenomena. *Mater Today* 15:320–327
- Rondinelli JM, May SJ, Freeland JW (2012) Control of octahedral connectivity in perovskite oxide heterostructures: an emerging route to multifunctional materials discovery. *MRS Bull* 37:261–270
- Rondinelli JM, Fennie CJ (2012) Octahedral rotation-induced ferroelectricity in cation ordered perovskites. *Adv Mater* 24:1961–1968
- Rondinelli JM, Spaldin NA (2011) Structure and properties of functional oxide thin films: insights from electronic-structure calculations. *Adv Mater* 23:3363–3381
- May SJ, Kim JW, Rondinelli JM, Karapetrova E, Spaldin NA, Bhattacharya A, Ryan PJ (2010) Quantifying octahedral rotations in strained perovskite oxide films. *Phys Rev B* 82:014110
- Vailionis A, Boschker H, Siemons W, Houwman EP, Blank DHA, Rijnders G, Koster G (2011) Misfit strain accommodation in epitaxial ABO<sub>3</sub> perovskites: lattice rotations and lattice modulations. *Phys Rev B* 83:064101
- Kumah DP, Disa AS, Ngai JH, Chen H, Malashevich A, Reiner JW, Ismail-Beigi S, Walker FJ, Ahn CH (2014) Tuning the structure of nickelates to achieve two-dimensional electron conduction. *Adv Mater* 26:1935–1940
- Johnson-Wilke RL, Marincel D, Zhu S, Warusawithana MP, Hatt A, Sayre J, Delaney KT, Engel-Herbert R, Schlepütz CM, Kim JW, Gopalan V, Spaldin NA, Schlom DG, Ryan PJ, Trolier-McKinstry S (2013) Quantification of octahedral rotations in strained LaAlO<sub>3</sub> films via synchrotron X-ray diffraction. *Phys Rev B* 88:174101
- May SJ, Smith CR, Kim JW, Karapetrova E, Bhattacharya A, Ryan PJ (2011) Control of octahedral rotations in (LaNiO<sub>3</sub>)<sub>n</sub>/(SrMnO<sub>3</sub>)<sub>m</sub> superlattices. *Phys Rev B* 83:153411
- Kinyanjui MK, Lu Y, Gauquelin N, Wu M, Frano A, Wochner P, Reehuis M, Christiani G, Logvenov G, Habermeier HU, Botton GA, Kaiser U, Keimer B, Benckiser E (2014) Lattice distortions and octahedral rotations in epitaxially strained LaNiO<sub>3</sub>/LaAlO<sub>3</sub> superlattices. *Appl Phys Lett* 104:221909
- He J, Borisevich A, Kalinin SV, Pennycook SJ, Pantelides ST (2010) Control of octahedral tilts and magnetic properties of perovskite oxide heterostructures by substrate symmetry. *Phys Rev Lett* 105:227203
- Borisevich AY, Chang HJ, Huijben M, Oxley MP, Okamoto S, Niranjan MK, Burton JD, Tsymbal EY, Chu YH, Yu P, Ramesh R, Kalinin SV, Pennycook SJ (2010) Suppression of octahedral tilts and associated changes in electronic properties at epitaxial oxide heterostructure interfaces. *Phys Rev Lett* 105:087204
- Kan D, Aso R, Kurata H, Shimakawa Y (2014) Unit-cell thick BaTiO<sub>3</sub> blocks octahedral tilt propagation across oxide heterointerface. *J Appl Phys* 115:184304
- Aso R, Kan D, Shimakawa Y, Kurata H (2014) Control of structural distortions in transition-metal oxide films through oxygen displacement at the heterointerface. *Adv Funct Mater* 24:5177–5184
- Aso R, Kan D, Shimakawa Y, Kurata H (2013) Atomic level observation of octahedral distortions at the perovskite oxide heterointerface. *Sci Rep* 3:2214
- Aso R, Kan D, Shimakawa Y, Kurata H (2014) Octahedral tilt propagation controlled by A-site cation size at perovskite oxide heterointerfaces. *Cryst Growth Des* 14:2128–2132
- Hwang J, Son J, Zhang JY, Janotti A, Van de Walle CG, Stemmer S (2013) Structural origins of the properties of rare earth nickelate superlattices. *Phys Rev B* 87:060101
- Hwang J, Zhang JY, Son J, Stemmer S (2012) Nanoscale quantification of octahedral tilts in perovskite films. *Appl Phys Lett* 100:191909
- Chaloupka J, Khaliullin G (2008) Orbital order and possible superconductivity in LaNiO<sub>3</sub>/LaMO<sub>3</sub> superlattices. *Phys Rev Lett* 100:016404
- Benckiser E, Haverkort MW, Brück S, Goering E, Macke S, Frano A, Yang X, Andersen OK, Christiani G, Habermeier HU, Boris AV, Zegkinoglou I, Wochner P, Kim HJ, Hinkov V, Keimer B (2011) Orbital reflectometry of oxide heterostructures. *Nat Mater* 10:189–193
- Wu M, Benckiser E, Haverkort MW, Frano A, Lu Y, Nwankwo U, Brück S, Audehm P, Goering E, Macke S, Hinkov V, Wochner P, Christiani G, Heinze S, Logvenov G, Habermeier HU, Keimer B (2013) Strain and composition dependence of orbital polarization in nickel oxide superlattices. *Phys Rev B* 88:125124

26. Boris AV, Matiks Y, Benckiser E, Frano A, Popovich P, Hinkov V, Wochner P, Castro-Colin M, Detemple E, Malik VK, Bernhard C, Prokscha T, Suter A, Salman Z, Morenzoni E, Cristiani G, Habermeier HU, Keimer B (2011) Dimensionality control of electronic phase transitions in nickel-oxide superlattices. *Science* 332:937–940
27. Frano A, Schierle E, Haverkort MW, Lu Y, Wu M, Blanco-Canosa S, Nwankwo U, Boris AV, Wochner P, Cristiani G, Habermeier HU, Logvenov G, Hinkov V, Benckiser E, Weschke E, Keimer B (2013) Orbital control of noncollinear magnetic order in nickel oxide heterostructures. *Phys Rev Lett* 111:106804
28. Jia CL, Lentzen M, Urban K (2003) Atomic-resolution imaging of oxygen in perovskite ceramics. *Science* 299:870–873
29. Jia CL, Urban K (2004) Atomic-resolution measurement of oxygen concentration in oxide materials. *Science* 303:2001–2004
30. Jia CL, Mi SB, Urban K, Vrejoiu I, Alexe M, Hesse D (2008) Atomic-scale study of electric dipoles near charged and uncharged domain walls in ferroelectric films. *Nat Mater* 7:57–61
31. Jia CL, Mi SB, Faley M, Poppe U, Schubert J, Urban K (2009) Oxygen octahedron reconstruction in the SrTiO<sub>3</sub>/LaAlO<sub>3</sub> heterointerfaces investigated using aberration-corrected ultrahigh-resolution transmission electron microscopy. *Phys Rev B* 79:081405
32. Lentzen M, Jahn B, Jia CL, Thust A, Tillmann K, Urban K (2002) High-resolution imaging with an aberration-corrected transmission electron microscope. *Ultramicroscopy* 92:233–242
33. Lentzen M (2006) Progress in aberration-corrected high-resolution transmission electron microscopy using hardware aberration correction. *Microsc Microanal* 12:191–205
34. Urban K, Jia CL, Houben L, Lentzen M, Mi SB, Tillmann K (2009) Negative spherical aberration ultrahigh-resolution imaging in corrected transmission electron microscopy. *Philos Trans R Soc A* 367:3735–3753
35. Glazer AM (1972) The classification of tilted octahedra in perovskites. *Acta Crystallogr Sect B* 28:3384–3392
36. Garcia-Munoz JL, Rodriguez-Carvajal J, Lacorre P, Torrance JB (1992) Neutron-diffraction study of RNiO<sub>3</sub> (R = La, Pr, Nd, Sm): electronically induced structural changes across the metal-insulator transition. *Phys Rev B* 46:4414–4425
37. Vasylechko L, Matkovskii A, Savytskii D, Suchocki A, Wallrafen F (1999) Crystal structure of GdFeO<sub>3</sub>-type rare earth gallates and aluminates. *J Alloys Compd* 291:57–65
38. Moon EJ, Balachandran PV, Kirby BJ, Keavney DJ, Sichel-Tissot RJ, Schlepütz CM, Karapetrova E, Cheng XM, Rondinelli JM, May SJ (2014) Effect of interfacial octahedral behavior in ultrathin manganite films. *Nano Lett* 14:2509–2514